Available online at www.sciencedirect.com

SciVerse ScienceDirect

Physics Procedia 37 (2012) 1373 – 1380

Physics Procedia

TIPP 2011 - Technology and Instrumentation in Particle Physics 2011

Progress in Development of Monolithic Active Pixel Detector for X-ray Astronomy with SOI CMOS Technology

Shinya Nakashima[a], Syukyo Gando Ryu[a], Takeshi Go Tsuru[a], Ayaki Takeda[b], Yasuo Arai[c], Toshinobu Miyoshi[c], Ryo Ichimiya[c], Yukiko Ikemoto[c], Toshifumi Imamura[d], Takafumi Ohmoto[d], Atsushi Iwata[d]

[a]*Department of Physics, Graduate School of Science, Kyoto University, Kitashirakawa Oiwake-cho, Sakyo-ku, Kyoto 606-8502, Japan*
[b]*Department of Particle and Nuclear Physics, Graduate School of High Energy Accelerator Science, The Graduate University for Advanced Studies (SOKENDAI), High Energy Accelerator Research Organization(KEK), 1-1 Oho, Tsukuba, Ibaraki 305-0801, Japan*
[c]*Institute of Particle and Nuclear Studies, High Energy Accelerator Research Org., KEK, Tsukuba 305-0801, Japan*
[d]*A-R-Tec Corp., Hiroshima Techno Plaza 405, 3-13-26 Kagamiyama, Higashi-Hiroshima 739-0046, Japan*

Abstract

We have been developing an active pixel sensor for X-ray astronomy. In this paper, we report on the design and the characterization of the recently-developed device named XRPIX1-FZ. We applied the high-resistivity Si wafer (∼7 kΩ cm) to the sensor layer for a thick depletion layer. The chemical-mechanical polishing, which we applied to smooth the rough backside of the Si wafer, successfully reduced the dark current. We used the single-pixel readout mode and achieved the energy resolution of 260 eV in FWHM at 8 keV. Moreover, we developed the 3 × 3 pixel readout mode for the evaluation of split events and confirmed the full depletion of 250 μm thick at the reverse-bias voltage of 30 V .

Keywords: SOI, pixel, X-ray imaging, X-ray spectroscopy

1. Introduction

X-ray charge-coupled devices (CCDs) are the standard imaging-spectrometers for the modern X-ray astronomy because of their small-size pixel (∼20 μm), fano-limited energy resolution (∼130 eV in FWHM at 6 keV), and the high detection efficiency over 0.3-10 keV band [1, 2, 3]. However, weak points of X-ray CCDs are the poor time resolution (a few seconds) and the low radiation tolerance due to the charge transfer. In addition, cosmic rays in the satellite orbit produce a high non–X-ray background which limits observations at the energy band above 10 keV.

We aim to achieve a low non–X-ray background (5×10^{-5} cts/s/keV/100 mm^2 at 20 keV in the low earth orbit) and a wide energy band (0.3–40 keV), in addition to the imaging and spectroscopic capabilities comparable to X-ray CCDs. For reduction of the non–X-ray background, an anti-coincidence system is useful (see figure 1 and [4]). The system consists of a main sensor and a surrounding active shield. An

Email address: shinya@cr.scphys.kyoto-u.ac.jp (Shinya Nakashima)

1875-3892 © 2012 Published by Elsevier B.V. Selection and/or peer review under responsibility of the organizing committee for TIPP 11. Open access under CC BY-NC-ND license. doi:10.1016/j.phpro.2012.04.100

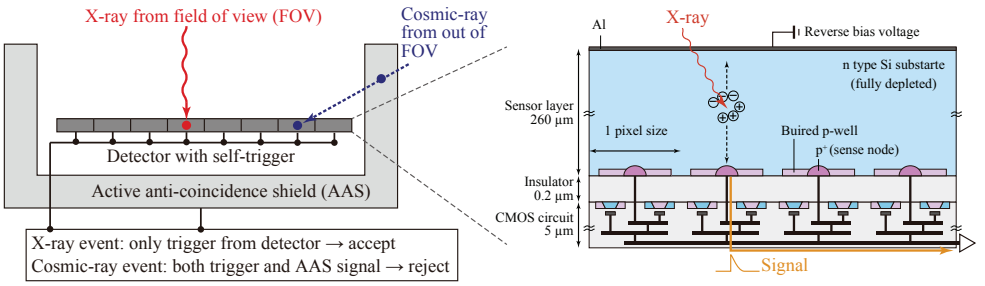

Fig. 1. Concept of the anti-coincidence system and the schematic view of the SOI sensor (cross section).

X-ray from the field of view is detected by only the main sensor, while a cosmic-ray is detected by both the main sensor and the active shield. Thus, we are able to extract X-ray events using anti-coincidence method with the main sensor and the active shield.

Recently, active pixel sensors (APSs) have been developing in various places because they have many advantages over X-ray CCDs. Each pixel in APSs has its own readout node and the charge transfer such as CCDs is not required. Thus, APSs not only are capable of random access readout but also have higher radiation tolerance. For example, one of the progressed APSs is DEPFET detector [5].

The readout speed of recent APSs is not sufficient for the background reduction even if it is much higher than that of CCDs. In order to realize the anti-coincidence readout, we need the self-trigger system detecting signals with time resolution of <10 μs. We focus on the silicon-on-insulator (SOI) wafer which is composed of a thick, high-resistivity Si substrate (sensor part) and a thin, low-resistivity Si layer (CMOS circuit) sandwiching a insulator (SiO_2) layer [6]. The schematic design of the detector is shown in figure 1. The sensor layer is fully depleted and an X-ray enters from the back side. A number of p+ (sense-nodes) are implanted at the sensor layer. Contact vias which connect the sense-nodes and the CMOS circuits are created in the insulator layer. Around the p+, we make the buried p-well in order to suppress the back-gate effect of the CMOS circuit [7]. Since MOSFETs made on the SOI wafer are separated from each other by the insulator, the SOI sensor has good performance in low parasitic capacitance, high-speed readout, and low power consumption. Our SOI sensor is also capable of radiation tolerance over 100 krad [8]. Thus, the total ionization dose effect in the insulator layer has little impact on our application in the low earth orbit (~0.6 krad/year and the typical operation time of ~10 years).

In 2010, we produced the first prototype detector named XRPIX1 which has the intra-pixel trigger. The details and the performance of XRPIX1 are reported in [9]. The trigger capability was confirmed by an optical laser. The readout noise and the energy resolution of the XRPIX1 was measured to be 129 e^- equivalent noise charge in rms and 1.4 keV in FWHM at 8 keV, respectively. Further suppression of the readout noise is necessary to achieve the fano-limited energy resolution. We also confirmed the depletion depth of 147 μm at the reverse-bias voltage ($V_{\rm bias}$) of 100 V. However, we have not achieved the full depletion (260 μm) due to the breakdown voltage of 120 V.

In order to achieve the full depletion at low $V_{\rm bias}$, a higher-resistivity Si for the sensor layer is required. Recently, we adopted the Floating Zone (FZ) wafer which has much higher resistivity. The new device using the FZ wafer is named XRPIX1-FZ.

In this paper, we focus on the spectroscopic performance of XRPIX1-FZ such as the dark current, the gain uniformity, the readout noise, and the depletion depth. We report on the results from a newly-introduced readout method for suppressing the readout noise.

2. Device Description

The chip design of XRPIX1-FZ is summarized in table 1. We used the 0.2 μm CMOS fully depleted SOI process provided by OKI Semiconductor Co. Ltd. The resistivity of the Si wafer for the sensor layer is ten

Table 1. Summary of the chip design

	XRPIX1	XRPIX1-FZ
Process	OKI 0.2 μm CMOS fully depleted SOI process	
Format	32 × 32 pixels	
Pixel size	30.6 μm square	
Window	Front-side illumination	
Resistivity of the sensor	0.7 kΩ cm	7 kΩ cm
CMP treatment	none	applied
Thickness of the sensor	260 μm	250 μm

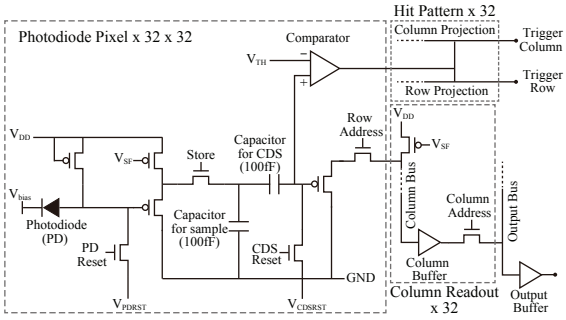

Fig. 2. Readout chain of XRPIX1-FZ.

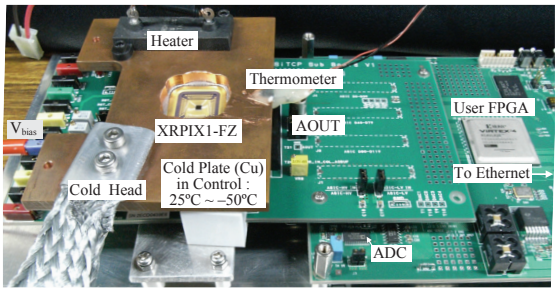

Fig. 3. Photo of the experimental setup.

times higher than that of XRPIX1. We applied the chemical-mechanical polishing (CMP) to the backside of the chip for smoothing the rough surface. After the CMP, the backside was spattered with Al (200 nm) for applying the bias voltage from the backside. The thickness of the sensor layer is 250 μm. Our goal is a back-side illumination sensor, but we have not achieved the full depletion. Thus, we used the device as a front-side illumination type.

The pixel circuitry of XRPIX1-FZ is entirely the same as that of XRPIX1 (figure 2). Each pixel has the correlated double sampling (CDS) function and the trigger function. The CDS circuit is for cancelling a reset noise from the sense-node capacitance. The trigger circuit is for outputs of a hit timing and a hit pattern. For evaluation, 32 × 32 pixels are separated into 4 blocks according to the different types of transistors and capacitors used in the CMOS circuit (see table I in [9]). In this paper, we focus on the block consisting of the body/source-tie type transistors and the metal-insulator-metal type capacitors.

3. Characterization of the Device

The experimental setup was same as that in the previous work (figure 3). We have controlled the chip temperature from 25 °C to -50 °C using a cooler and a heater. In the following evaluation tests, we kept the chip temperature at -50 °C unless otherwise noted. The setup was in the vacuum chamber which was in the condition of $\sim 10^{-6}$ torr. Since the full depletion of the sensor layer has not been confirmed yet, X-rays were irradiated from the side of the CMOS layer (front-side illumination).

We used the readout method of frame-by-frame readout mode according to [9]: signals from all the pixels are read out sequentially after reset and waiting for X-ray injections during the predetermined exposure time (integration time). A dataset taken from one exposure time is called a frame. In this paper, exposure time was set as 1 ms unless otherwise noted. A base level (pedestal) of each pixel is determined by averaging the data in absence of X-ray injection. The difference between the signal level when an X-ray is injected and the base level corresponds to the X-ray energy.

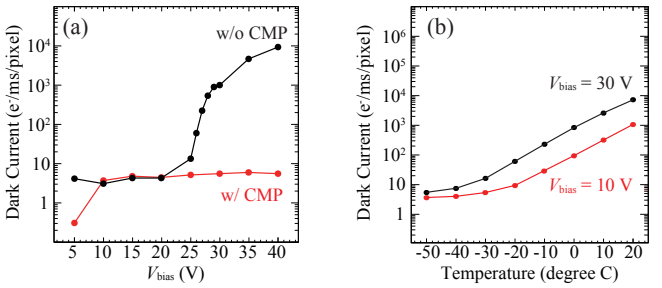

Fig. 4. Dependence of the dark current to the $V_{\rm bias}$ (a) and the temperature (b). The horizontal axis are liner scales while the vertical axis are logarithmic scales. The unit of the vertical axis is obtained from the conversion of the output voltages by using the gain measured in section 3.2. The lines connecting the date points are only eye guide.

3.1. Dark current

During the integration time, a dark current flows into the sense node and increases the output voltage. The output voltage is proportional to the integration time under the condition of no X-ray injection. We observed the change of output over an 1000 ms exposure. The gradient of the output voltage is calculated from the fitting with a linear function. We investigated the dark current of XRPIX1-FZ at different $V_{\rm bias}$ and temperatures.

Figure 4a shows the dependence of the dark current on $V_{\rm bias}$. In the chip without the CMP, the dark current increases sharply at $V_{\rm bias}$ = 25 V. Given the results in section 3.5, we conclude that the depletion region reaches the back side of the sensor layer and defects at the surface of the Si substrate cause a large amount of the dark current. The figure indicates that applying the CMP reduced the dark current significantly. However, the dark current of our device (6 e/ms/pixel $\simeq$ 100 pA/cm^2 at -50 °C) is still a few orders of magnitude larger than that of the X-ray CCD which is going to be carried on the next japanese satellite *Astro-H* ($\sim$0.2 pA/cm^2 at -50 °C. Takeshi. Go. Tsuru, private communication). One of the possible cause might be due to the bonding process of the handle wafer to the BOX layer. We will investigate further the source of the dark current.

Figure 4b is the dependence of the dark current on the working temperature measured by the chip with CMP . It follows the exponential curve down to -20 °C, which is consistent with the dependence of generation current. On the other hand, the plateau under -20 °C is observed. This reason is not clear and a further investigation is necessary.

3.2. Gain

We investigated the response of XRPIX1-FZ to several energies of X-rays. $V_{\rm bias}$ was set as 30 V. Figure 5a is the raw spectrum of the Cu-K line ($\sim$8 keV) and the Mo-K line ($\sim$17 keV) characteristic X-rays. In this spectrum, we collected the all-pixels data of 4×10^5 frames; the effective exposure time is 400 s. We see that Cu and Mo peaks are resolved.

Figure 5b shows the relationship between the incident–X-ray energies and the output voltages obtained from the resolved X-ray peaks. Its slope shows the gain of 3.3 μV/e$^-$, since 1 e$^-$ is produced per 3.65 eV in the Si detector. The obtained gain is close to that of XRPIX1. Adopting the same circuit gain of 0.91 for the source followers and buffers as that of XRPIX1 [9], the sense-node capacitance is calculated to be 44fF. The readout noise and the energy resolution are 120 e$^-$ rms and 1.5 keV in FWHM at 8 keV, respectively, which are the same as those of XRPIX1.

We also made the X-ray spectrum of each pixel and measured the gain uniformity among the pixels. The result is shown in figure 5c. The standard deviation of the gain distribution is 1%.

3.3. Suppressing the Readout Noise

The readout noise of 120 e$^-$ rms found in section 3.2 is much higher than the fano-limited energy resolution. As reported in [9], the readout noise consists of the kT/C noise (reset noise) from the CDS

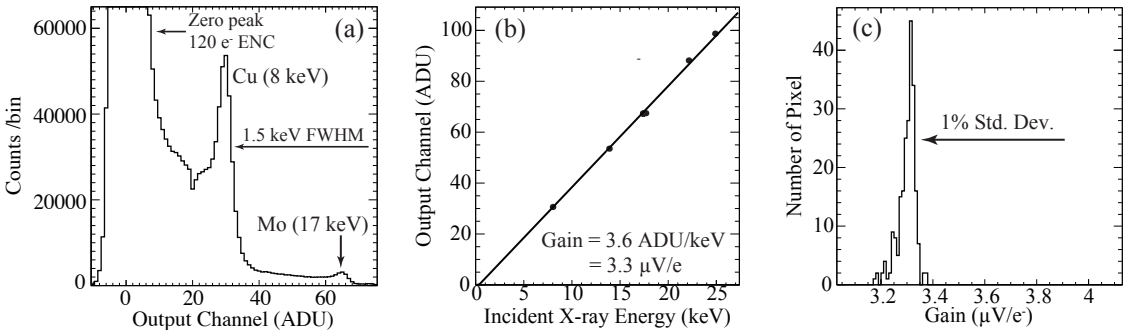

Fig. 5. (a) X-ray spectrum obtained from XRPIX-FZ. ADU represents the output from the digital-analog convertor. 1 ADU is equal to 248 μV. (b) Calibration between X-ray energies (keV) and output voltages in ADU. (c) Gain distribution of all pixels.

capacitance (60 e^- rms), the noise from the source followers and the column buffer (95 e^- rms), and the noise from peripheral readout system (e.g., ADC, power supply. 61 e^- rms). The suggestion for the noise reduction is also described in [9]. In order to evaluate other device characteristics in the limited noise performance, we used the single-pixel readout mode (see Ⅲ-A in [10]), which is not for the normal operation but useful for the evaluation test. In this mode, we continuously read out the output voltages of a single pixel in the following steps.

Step 1. Reset the sense-node voltage.
Step 2. Make continuous 1024 readout of the one pixel with the sampling rate of 1 MHz. X-ray detection is made in during this step.
Step 3. Return to Step 1.

Figure 6a shows a typical dataset of a cycle with an X-ray injection. The positive edge corresponds to the timing of the X-ray injection. The energy of an incident X-ray is represented by the difference between the signal level and the base level. The base level and the signal level is calculated from the average of 80-successive voltages before and after the edge, respectively. Since there is no reset in this processing, signal is not affected by the reset noise. Furthermore, the average computation suppresses the high-frequency components of both the transistor noise (white noise) and the external noise (i.e., low-pass filter). In the analyses, we set threshold of an X-ray detection (the event threshold) to the 5-ADU jump. If no X-ray is detected, we calculate the difference between the average of 80-successive voltages before and after the 500th sample in the cycle. This procedure makes a peak around zero and the width of this peak is equal to the readout noise.

Figure 6b shows the spectrum obtained from the above method. We collected the data of 4×10^5 cycles. The dip around 5 ADU (right of the zero peak) is due to the event threshold. The readout noise calculated from the zero-peak is 23 e^- rms. The difference of the readout noise between the single-pixel readout mode and the frame-by-frame readout mode is $\sqrt{120^2 - 23^2} = 118$ e^- rms. Since the kT/C noise of 60 e^- rms is completely cut off, remaining $\sqrt{118^2 - 60^2} = 101$ e^- rms is the high-frequency component of the transistor noise and the external noise, which is effectively reduced to 23 e^- rms by the averaging computation.

The Cu-Kα and -Kβ lines are clearly resolved. We obtained the best energy resolution in our device of 260 eV in FWHM at the Cu-Kα line. The fano-noise at the energy of the Cu-Kα line is converted to 137 eV in FWHM. The readout noise of 23 e^- rms is also converted to 197 eV in FWHM. The sum of the two noise is consistent with the observed resolution of 260 eV.

Since signal charges diffuse during the traveling through the depletion region to the sense node, it is possible that the signal charge spreads into neighboring pixels; this is called a split event. The tail like structure shown in figure 6 is most likely due to split events as same as the case of X-ray CCDs (e.g., [11]).

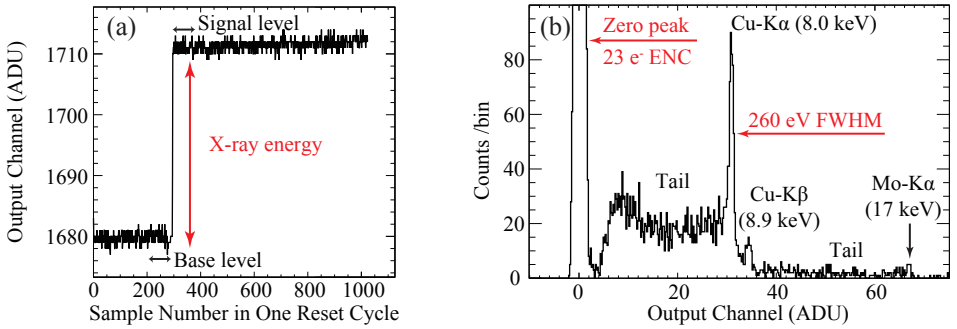

Fig. 6. (a) Sequential 1024 samples in one rest cycle with an X-ray injection. (b) Spectrum obtained by the single-pixel readout mode.

3.4. Evaluation of Split Events

In order to evaluate incident–X-ray energy precisely, we need to sum all the split signals. Thus, we developed the new readout method named "3 × 3 pixel readout mode", in which we focused on a single 3 × 3 pixel cluster. These pixels are read out in the following steps.

Step 1. Reset the sense-node voltages.

Step 2. Read out the signals from the 1st pixel to the 9th pixel cyclically (i.e. 1st → 2nd → ⋯ → 9th → 1st → 2nd → ⋯) until 113 samples per pixel are obtained. Since we switch between 9 pixels with one 1 MHz ADC, the effective sampling rate for each pixel is 1/9 MHz.

Step 3. Return to Step 1.

Figure 9 is 9-pixel dataset in one reset cycle with an X-ray injection. We see that the center and the right pixel show the edge structures at the same timing; it is a split event. As the reference value of an X-ray detection, we used the event threshold for the center pixel while the split threshold for the surrounding pixels. We empirically determined the event threshold and the split threshold as 5 ADU and 1.2 ADU, respectively. We named the surrounding pixels of exceeding the split threshold as split pixels. We evaluated the signals of the center pixel and the split pixels in the same way as the single-pixel readout mode. However, we used the average of 20 samples for the estimation of the signal and base levels because the sampling number in each pixel is 113. After that, we sorted the events according to the split pattern as shown in figure 8.

The branching ratio at $V_{\rm bias}$ = 30 V was single pixel 27%, double pixels 37%, triple pixels 12%, quadruple pixels 5%, and the others 9%. We obtained X-ray spectra from the events of single pixel, double pixels, triple pixels and quad pixels by summing the outputs of the center pixel and the split pixels. The events of "the others" were not used in the following spectral analyses.

Figure 9 shows the spectrum obtained from the 3 × 3 pixel readout mode. We collected the data of 1 × 10^6 cycles. The blue line in figure 9 shows the spectrum of "single pixel" events. We investigated this spectrum for comparison with that from the single pixel readout mode. The readout noise was measured by the same way of the single-pixel readout mode using the center pixel of the 3 × 3 pixel date without an X-ray detection. The readout noise and the energy resolution are decrease to 33 e^- rms and 343 eV, respectively (c.f., section 3.3). It is considered to be due to the difference of the effective sampling rate and the sample number of the average computation.

The red line in figure 9 shows the spectrum of the all selected events of "single pixel", "double pixels", "triple pixels", and "quad pixels". While the counts of the events become higher than those of "single pixel" for both the Cu-K and Mo-K lines, the its ratio is higher in the Mo-K than Cu-K. This is because that high-energy X-rays tend to be absorbed in the deep point of the depletion layer and split charges between pixels. The energy resolution at the Cu-Kα line is 504 eV in FWHM, which is worse than that of "single pixel". It is due to the summing computation of split events. The effects of the summing multi pixels are simply estimated as 343 × $\sqrt{2}$ = 484 eV since "double pixels" are dominant. We also evaluated the equivalent width for the 8 keV line from the recombined event spectrum. The total count of the 8 keV line is obtained

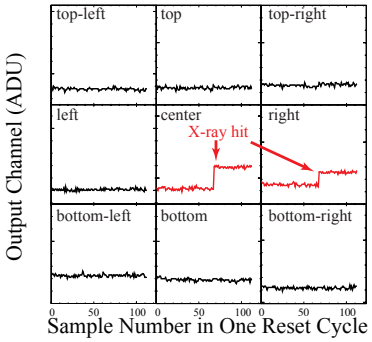

Fig. 7. Sequential 113 samples of the 3x3 pixels. The 9 panels are aligned in accordance with the relative pixel position. The vertical-axis values in the each panel are different but scaled: one tick mark shows 10 ADU.

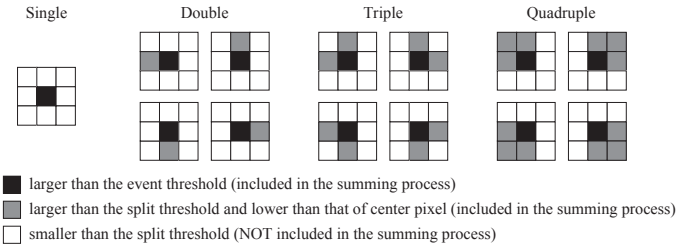

Fig. 8. Diagram for the selection of split events.

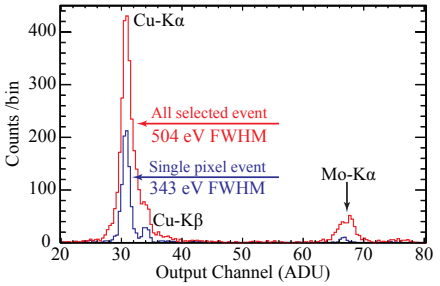

Fig. 9. Spectrum obtained from the 3 × 3 pixel mode. The blue line shows the spectrum composed of only single event while the red line composed of all selected events.

from the fitting with a gaussian (865 counts). The background which is due to incomplete charge collection is estimated by the average count in the energy range between 2 keV and 5 keV (5.7 counts/keV). Then, the equivalent width for the 8 keV line is evaluated as 150 keV. This value is worse than that of other APSs by a few factors (ex. ~510 keV from [5]). The methods to improve the charge collection efficiency is under investigation.

We also evaluated a peak to background ratio of the recombined event spectrum. The background which is due to incomplete charge collection is estimated by the average count in the energy range between 2 keV and 5 keV. Then, the ratio of the peak height of the 8 keV line to the background is evaluated as 300. This value is a order of magnitude worse than other APSs (ex. [5]). The methods to improve the charge collection efficiency is under investigation.

3.5. Depletion Depth

Using the data of 3 × 3 pixel readout mode, we measured the depletion depth as a function of $V_{\rm bias}$ following the same method described in [9]. We irradiated the chip with the well-calibrated X-rays of Cu-Kα (~8 keV) and Mo-Kα (~17 keV) lines simultaneously. The 8 keV and 17 keV X-ray has a different attenuation length. Thus, we calculated the depletion depth from the ratio of the detected 17 keV counts to 8 keV counts.

The result is shown in figure 10. The red line in figure 10 indicates the predicted depletion depth (W) written as,

$$W = \sqrt{2\epsilon\mu\rho(V_{\rm bias} + V_{\rm i})} \quad (1)$$

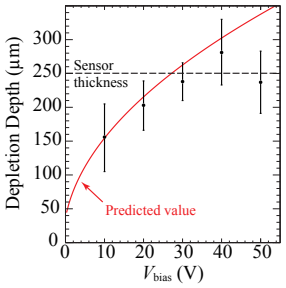

Fig. 10. Dependence of depletion depth to $V_{\rm bias}$. The red line is the predicted value obtained from Eq. 1. The sensor thickness of 250 μm is shown in the dashed line.

where ϵ, μ, ρ, and $V_{\rm i}$ are the permittivity (1.036×10^{-12} F/cm,), the electron mobility (1500 cm^2/s/V), the resistivity of the Si wafer (7 kΩ cm), and the intrinsic bias voltage due to the p-n junction ($\sim$ 0.6 V), respectively. The experimental result on the depletion layer matches the prediction below 30 V and becomes constant above 30 V, which suggests that full depletion of 250 μm is achieved at $V_{\rm bias}$ = 30 V.

4. Summary

We have developed XRPIX1-FZ which has the high-resistivity ($\sim$7 kΩ cm) Si wafer for a thick depletion layer. We successfully reduced the dark current with the CMP of the Si substrate. The gain dispersion among the pixels is 1% in standard deviation. We demonstrated the energy resolution of 260 eV at 8 keV in the single-pixel readout mode. We evaluated the split events with the 3×3 readout mode and confirmed the full depletion of the sensor layer (250 μm). Thus, the test of a back illumination is a next issue.

Acknowledgement

This work is supported by Grant-in-Aids from the Ministry of Education, Culture, Sports, Science and Technology (MEXT) of Japan, Scientific Research B, No 20340043 and 23340047, and ISAS/JAXA, Tou-saikiki Kisokaihatsu Jikkenhi (TGT). SN and SGR are supported by JSPS Research Fellowship for Young Scientists.

References

[1] K. Koyama *et al*., X-ray imaging spectrometer (XIS) on board suzaku, PASJ 59 (2007) S23–S33.
[2] G. P. Garmire *et al*., Advanced CCD imaging spectrometer (ACIS) instrument on the Chandra X-ray Observatory, in: Society of Photo-Optical Instrumentation Engineers (SPIE) Conference Series, Vol. 4851 of Society of Photo-Optical Instrumentation Engineers (SPIE) Conference Series, 2003, pp. 28–44.
[3] M. J. L. Turner *et al*., The European Photon Imaging Camera on XMM-Newton: The MOS cameras, A&A 365 (2001) L27 – L35.
[4] T. Takahashi *et al*., Newly developed low background hard X-ray/gamma-ray telescope with the well-type phoswich counters, Nuclear Science, IEEE Transactions on 40 (4) (1993) 890–898.
[5] A. Meuris *et al*., Development and Characterization of New 256 × 256 Pixel DEPFET Detectors for X-Ray Astronomy, Nuclear Science, IEEE Transactions on 58 (3) (2011) 1206 –1211. doi:10.1109/TNS.2011.2126599.
[6] Y. Arai *et al*., Monolithic pixel detector in a 0.15 μm SOI technology, in: Nuclear Science Symposium Conference Record, 2006. IEEE, Vol. 3, 2006, pp. 1440–1444.
[7] Y. Arai *et al*., Development of SOI pixel process technology, Nuclear Instruments and Methods in Physics Research Section A 636 (1, Supplement 1) (2011) S31 – S36.
[8] Y. Onuki *et al*., SOI detector developments, in: PoS(Vertex 2011)043, 2011.
[9] S. G. Ryu *et al*., First performance evaluation of an X-ray SOI pixel sensor for imaging spectroscopy and intra-pixel trigger, Nuclear Science, IEEE Transactions on 58 (5) (2011) 2528 –2536. doi:10.1109/TNS.2011.2160970.
[10] G. Prigozhin *et al*., Characterization of Three-Dimensional-Integrated Active Pixel Sensor for X-Ray Detection, Electron Devices, IEEE Transactions on 56 (11) (2009) 2602 –2611.
[11] M. W. Bautz *et al*., Progress in X-ray CCD sensor performance for the Astro-E2 X-ray imaging spectrometer, in: Society of Photo-Optical Instrumentation Engineers (SPIE) Conference Series, Vol. 5501, 2004, pp. 111–122.